Showcasing research from Professor Sangmin Jeon's laboratory, Pohang University of Science and Technology (POSTECH), Pohang, Gyeongbuk, Republic of Korea.

Synergistic effect of a berlin green framework for highly efficient moisture-electric energy transformation

We developed a novel moisture-induced power generator (MPG) utilizing Berlin green (BG) for enhanced moisture-electric energy transformation (MEET) performance. The MPG device features a bilayer structure with a BG/graphene oxide/cellulose nanofiber composite layer on NaCl/cellulose nanofiber composite layer. Moisture adsorption triggered the dissociation and spontaneous diffusion of sodium ions, generating electricity. Furthermore, the insertion of sodium ions into the BG framework reduced BG to Prussian blue, generating additional electricity. This synergistic interplay resulted in excellent MEET performance: 1.17 V and 2770 μA cm^{-2} at 90% relative humidity.

ROYAL SOCIETY
OF **CHEMISTRY**

rsc.li/ees

ROYAL SOCIETY
OF CHEMISTRY

PAPER

Check for updates

Synergistic effect of a Berlin green framework for highly efficient moisture-electric energy transformation†

Minjae Song,‡ Daewoong Kim,‡ Hyewon Lee, Hyunsoo Han and Sangmin Jeon ⓘD *

We developed a novel moisture-induced power generator (MPG) by utilizing Berlin green (BG) as an active material to enhance its moisture-electric energy transformation (MEET) performance. The bilayer-based MPG device was fabricated by stacking a BG/graphene oxide/cellulose nanofiber (BGC) composite layer on a NaCl/cellulose nanofiber (NC) composite layer. Moisture adsorption onto the NC layer triggered the dissociation and spontaneous diffusion of the sodium ions toward the BGC layer due to the ion concentration gradient. The adsorption of positive sodium ions onto the BGC layer induced electron transfer from the counter electrode through the external wire, generating electricity. Furthermore, the insertion of sodium ions into the BG framework reduced BG to Prussian blue, generating additional electricity. This synergistic interplay of physical and electrochemical processes resulted in excellent MEET performance: 1.17 V and 2770 $\mu A\ cm^{-2}$ at 90% relative humidity. These values are two and ten times higher than those of the bilayer MPG without BG, respectively. In particular, the current density of BGC–NC is the highest value that has been reported to date.

Broader context

A water wheel was the first method of generating mechanical energy to replace human labor since the dawn of human civilization, evolving into water turbines during the industrial revolution period. Despite its wide applicability, it required rotating parts and operated only with the presence of water flow. This limitation was addressed by moisture-induced power generators (MPGs), which harness ambient moisture-ubiquitous and always present-to produce electrical energy without any rotating parts. While MPGs offer the advantages of ubiquity, simplicity, and direct current output, conventional MPGs have focused only on generating non-faradaic currents, with resulting current densities far below the values required for practical applications ($>1\ mA\ cm^{-2}$). For the first time, we utilized electrochemically active materials (Berlin Green) to generate both non-faradaic and faradaic currents. Notably, the resulting current density is the highest reported to date.

Introduction

Moisture-induced power generators (MPGs) are regarded as a promising energy-harvesting technology that harnesses atmospheric moisture to produce electrical energy.[1,2] MPGs are constructed using hygroscopic materials that contain dissociable functional groups or deliquescent salts that spontaneously absorb moisture and produce hydrated ions.[3–5] The ion concentration gradient established during fabrication or asymmetric moisture adsorption leads to ion migration,[6–8] which generates a potential difference, causing electrons to move through an external

circuit.[9,10] Although MPGs offer many advantages, such as ubiquity, simplicity, spontaneity, and direct current output, their moisture-electric energy transformation (MEET) performance must be enhanced to expand their practical applications.[11,12]

Two strategies are commonly used to enhance MEET performance: creating an ion concentration gradient and facilitating ion transport. Qu *et al.* created an ion concentration gradient by asymmetrically impregnating sulfonic acid into a textile scaffold.[13] Li *et al.* improved ion transport by employing lithium ions to disrupt the hydrogen bonding network of polymer chains, thereby increasing the spacing between them.[14] However, both approaches were based on generating non-faradaic currents, and the resulting current densities were far below the value required for practical applications ($>1\ mA\ cm^{-2}$).[15] To address the high demand for enhanced MEET performance, it is necessary to utilize faradaic currents that can be spontaneously generated once moisture is adsorbed.

Department of Chemical Engineering, Pohang University of Science and Technology (POSTECH), 77 Cheongam-Ro, Pohang, Gyeongbuk, Republic of Korea.
E-mail: jeons@postech.ac.kr

† Electronic supplementary information (ESI) available. See DOI: https://doi.org/10.1039/d4ee00777h

‡ These authors contributed equally to this work.

In this study, we used Berlin green (BG) as the active material to develop a novel MPG that can generate both faradaic and non-faradaic currents. BG, an oxidized form of Prussian blue (PB), is cost-effective, easily synthesized, and chemically modifiable.[16,17] The BG-based MPG was prepared by stacking a BG/graphene oxide (GO)/cellulose nanofiber (CNF) (hereinafter abbreviated as BGC) composite layer on a NaCl/CNF (NC) composite layer. The adsorption of moisture onto the NC layer causes the sodium ions to dissociate and spontaneously diffuse toward the BGC layer because of the ion concentration gradient. The adsorption of positive sodium ions onto the BGC layer produces non-faradaic currents, whereas the insertion of sodium ions into the BG framework produces faradaic currents through the electrochemical reduction of BG to PB. This synergistic effect resulted in a high record-breaking current density of 2770 μA cm^{-2} at 90% RH. Additionally, we demonstrated that five BG-based MPGs (size: 6 mm $\times$ 6 mm each) connected in series were sufficient to power a digital calculator and an ultraviolet (UV) LED at 90% RH without any capacitors.

Experimental

Materials

NaCl ($>$99%) and hydrochloric (HCl) acid solution (35 wt%) were purchased from Samchun Chemistry Co. Ltd. (Seoul, Korea). Iron(III) chloride hexahydrate (FeCl$_3$·6H$_2$O; $>$99%), sodium borohydride (NaBH$_4$; $>$99%), GO, potassium ferricyanide (K$_3$Fe(CN)$_6$; $>$99%), and sodium ferrocyanide decahydrate (Na$_4$Fe(CN)$_6$·10H$_2$O; $>$99%) were procured from Sigma-Aldrich (St. Louis, MO). TEMPO-oxidized CNF powder and Petrifilms for *Escherichia coli* (*E. coli*) O157:H7 cultivation were purchased from ANPOLY Inc. (Pohang, Korea) and 3M (Saint Paul, MN), respectively. Deionized (DI) water was obtained using a reverse osmosis system (18.3 MΩ cm).

Preparation of BG and PB

BG (Fe(Fe(CN)$_6$)) particles were synthesized by adding 4 mmol of K$_3$Fe(CN)$_6$ to 100 mL of the 0.1 M HCl solution. The mixture was heated to 80 °C on a hot plate and stirred vigorously for 4 h. The resulting dispersion was centrifuged at 12 000 rpm for

30 min. Thereafter, the supernatant was removed, and the precipitate was rinsed with DI water. The precipitate was dried on a hot plate at 60 °C to obtain BG powder. PB (Na$_{1.46}$Fe(Fe(CN)$_6$)) was synthesized by reacting a 100 mL dispersion containing 1 mmol of the BG particle with excess NaBH$_4$ (20 mmol) at room temperature under rapid stirring for 1 h to facilitate further reduction. The resulting dispersion was rinsed and dried on a hot plate at 60 °C to obtain PB powder. X-Ray diffraction (XRD; Bruker) was performed to assess the crystallinity and internal structure of BG.

Preparation of BGC–NC bilayer membranes

NC membranes were produced by adding NaCl to a 0.5 wt% CNF solution (NaCl:CNF mass ratio = 4:1), followed by freeze-drying. BGC membranes were prepared by incorporating the BG and GO powders into a 0.5 wt% CNF solution (BG:GO:CNF mass ratio = 6:5:1) and then freeze-drying the mixture. Similarly, PB/GO/CNF (PGC) membranes were prepared with a PB:GO:CNF mass ratio of 6:5:1. The BGC–NC bilayer-based MPG (BGC–NC) was fabricated by stacking the BGC layer on the NC layer and pressing it with a 10 MPa load for 20 min at 70 °C. This process produced an asymmetric structure along the thickness. For comparison, GC–NC bilayer-based MPG (GC–NC) and PGC–NC bilayer-based MPG (PGC–NC) were fabricated.

Characterization of BGC–NC bilayer membranes

The morphologies and elemental compositions of the samples were analyzed using an X-ray photoelectron spectrometer (XPS, Nexsa G2, Thermo Fisher Scientific, MA) and a scanning electron microscopy with energy-dispersive X-ray spectroscopy (SEM-EDS; JSM-7800F PRIME, JEOL). The zeta potentials of BGC and GC when dispersed in DI water were measured using a Zetasizer Nano ZS (Malvern Instruments). The light reflectance spectra were acquired using a UV-visible spectrometer (Perkin-Elmer, Lambda 365).

Instrument setup for performance evaluation

Scheme 1a and b show the schematic and the optical image of BGC–NC bilayer-based MPG device, respectively. Gold-deposited stainless-steel (Au@SS) plates were used as inert current-collecting electrodes for the top and bottom surfaces
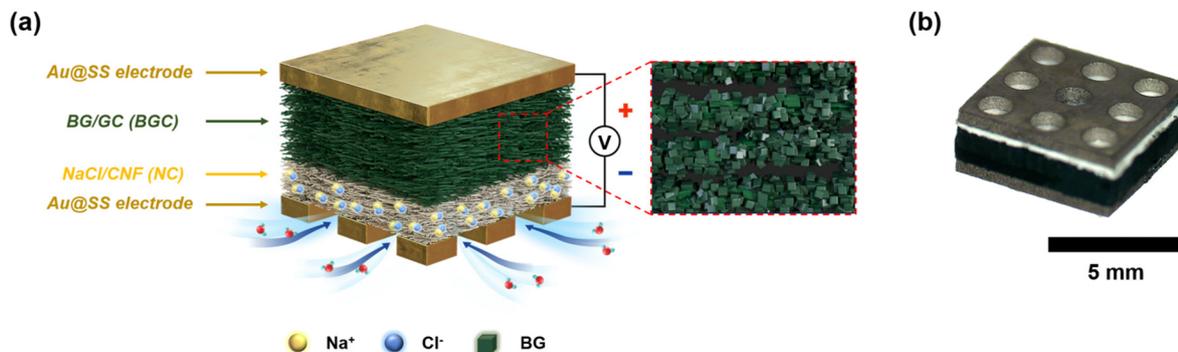
Scheme 1 (a) Schematic and (b) optical image of the BGC–NC bilayer-based MPG device. The area within the red dotted box is magnified to show the structure of the BGC layer.

5422 | *Energy Environ. Sci.*, 2024, **17**, 5421–5428

This journal is © The Royal Society of Chemistry 2024

of the bilayer membrane, respectively. The bottom electrode (6 mm × 6 mm) contained 9 holes (1 mm in diameter) that allowed for exposure to humid air. The electrodes were connected to conductive silver wires, and the device was securely positioned between two acryl plates. The bottom acrylic plate has a hole (5 mm × 5 mm) in the center to allow moisture access to the device. Two nonconductive clips were used to ensure optimal ohmic contact between the electrode and the BGC–NC bilayer membrane. The MEET performance of the device was evaluated using a homebuilt flow cell. The relative humidity (RH) of the flow cell was regulated by controlling the flow rates of the dry and wet nitrogen gas streams using mass flow controllers. The flow cell was kept at room temperature. The open-circuit voltage (V_{OC}) and short-circuit current (I_{SC}) were measured using a DMM7510 multimeter (Keithley Instruments, Cleveland, OH). To investigate the electrochemical reactions in BGC, cyclic voltammetry (CV) measurements were conducted using CompactStat (Ivium technologies, Netherlands).

Results and discussion

Characteristics of BGC–NC bilayer membranes

Fig. 1a and b show the SEM image and XRD pattern of the crystalline BG particles, respectively. The presence of XRD peaks corresponding to the (200), (220), (400), and (420) planes indicates that the crystalline structure of the BG particles is face-centered cubic.[17–19] Fig. 1c and d show the cross-sectional SEM image and corresponding EDS elemental mapping image of the BGC–NC bilayer with thicknesses of 0.2 mm (NC) and

1.1 mm (BGC). The yellow and orange colors represent sodium and iron, respectively, confirming the successful impregnation of NaCl into the NC layer and BG in the BGC layer. NaCl and BG were incorporated as crystalline particles with sizes of ∼0.5 and ∼1 μm, respectively, into each layer (Fig. S1, ESI†). The small size of the BG particles, which increases in adsorption sites, facilitates the efficient insertion of migrated sodium ions. Similarly, the small size of the NaCl particles enhances sodium ion release upon moisture adsorption.

Power outputs of BGC–NC

The power output of the MPGs was evaluated after installing them inside a flow cell. Fig. 2a shows the time-dependent changes in the open-circuit voltage of GC–NC and BGC–NC at 90% RH for 3 h. Upon exposure to humid air, both MPGs exhibited an increase in their voltage outputs due to the migration of Na$^+$ ions along the thickness direction. The maximum voltage output of BGC–NC (1.28 V) was higher than that of GC–NC (0.55 V), indicating the positive impact of BG particles on voltage generation. Fig. 2b shows the time-dependent changes in the short-circuit current densities of GC–NC and BGC–NC at 90% RH for 3 h. BGC–GC exhibited a maximum current density of 2910 μA cm^{-2}. Although its current density decreased from its peak value, it remained at 140 μA cm^{-2} even after 10 h (Fig. S2, ESI†). Conversely, GC–NC exhibited a considerably low current density output, with a maximum value of 283 μA cm^{-2}, indicating that BG particles have a positive effect on current generation. Next, BGC–NC was connected to various external resistors to further investigate its
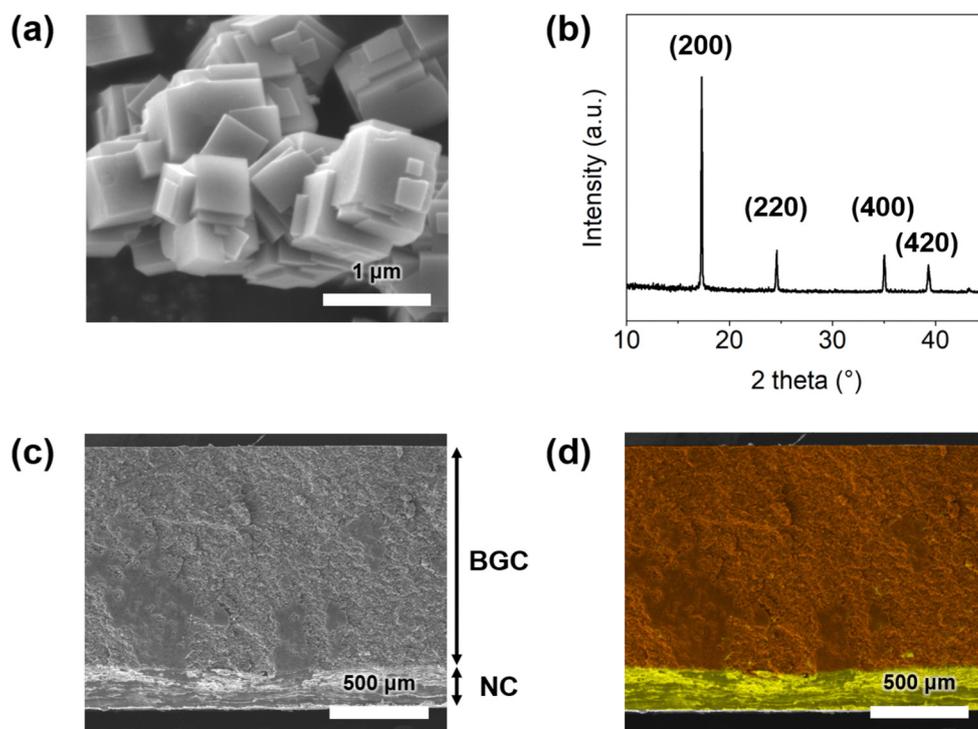

Fig. 1 (a) SEM image and (b) XRD pattern of the BG particles. (c) Cross-sectional SEM image and (d) corresponding EDS elemental mapping overlay image of the BGC–NC bilayer: sodium (yellow) and iron (orange).
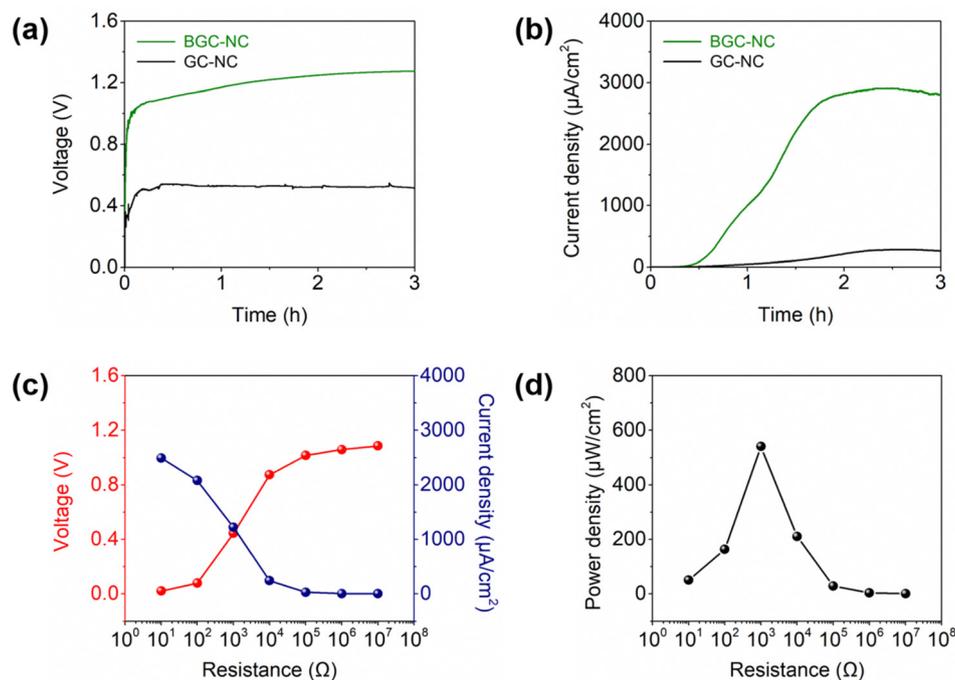
This journal is © The Royal Society of Chemistry 2024

Energy Environ. Sci., 2024, **17**, 5421–5428 | **5423**

Fig. 2 Time-dependent changes in the (a) open-circuit voltage and (b) short-circuit current density of GC–NC (black) and BGC–NC (green) at 90% RH for 3 h. (c) Voltage (red), current density (blue), and (d) areal power density of BGC–NC measured at different external load resistances.

applicability as a practical power source. Fig. 2c and d show the voltage–current density and power density outputs of BGC–NC at various load resistances of 10 Ω to 10 MΩ, respectively. As the load resistance increased from 10 Ω to 10 MΩ, the voltage increased from 0.02 V to 1.09 V, whereas the current density decreased from 2490 $\mu A\ cm^{-2}$ to 0.3 $\mu A\ cm^{-2}$. The highest power density and gravimetric energy density achieved were 541 $\mu W\ cm^{-2}$ and 9.05 Wh kg^{-1}, respectively, at a resistance of 1 kΩ.

MEET mechanism of BGC–NC

Fig. 3a illustrates the MEET mechanism of BGC–NC. When humid air is introduced into the bottom side of BGC–NC, the adsorbed water molecules dissociate NaCl to Na^+ and Cl^-. The resulting Na^+ ion concentration gradient along the thickness direction causes the Na^+ ions to move from the NC layer to the BGC layer. Because the BGC surface carries negative charges (−57.8 mV) due to the presence of carboxyl (–COO^-) and cyano (–CN^-) functional groups (Fig. S3, ESI†), these negative charges facilitate the selective migration of cations, creating a potential difference between the electrodes connected to BGC and NC. Fig. 3b compares the cross-sectional EDS mapping images of BGC–NC before and after moisture exposure, demonstrating the migration of the Na^+ ions into BGC. These Na^+ ions are either physically adsorbed onto GC/BG (resulting in a positively charged surface) or inserted into the BG framework (resulting in the electrochemical reduction of Fe^{3+} to Fe^{2+}), leading to the generation of non-faradaic or faradaic currents, respectively.

To evaluate the contributions of the non-faradaic and faradaic currents, a control experiment was conducted using a PGC composite layer in place of the BGC layer. Although PB and BG have the same structural backbone, they have different

oxidation states of coordination iron and sodium contents. While the voltage (0.65 V) and current (1070 $\mu A\ cm^{-2}$) outputs of PGC–NC were higher than those of GC–NC due to the presence of additional sites for the physical adsorption of Na^+ ions, they were lower than those of BGC–NC (Fig. S4, ESI†). The remarkable MEET performance of BGC–NC is attributed to the electrochemical redox reaction induced by the insertion of Na^+ ions into BG, which results in the reduction of Fe^{3+} ions to Fe^{2+} ions. The transformation of BG into PB after the current generation is visually evident from the color change (inset of Fig. 3c). BG exhibits a green color due to charge transfer between the Fe^{3+} and CN^- ligands, whereas PB exhibits a blue color due to charge transfer between the Fe^{2+} and CN^- ligands. Fig. 3c compares the UV-visible light reflectance spectra of BGC before and after power generation. After 3 h of current generation at 90% RH, the broad peak shifted from 540 nm to 456 nm, corresponding to the change from green to blue. In addition, XPS analysis of BGC–NC was performed to demonstrate that the reduction of Fe^{3+} ions to Fe^{2+} ions occurred during power generation (Fig. 3d). An increase in the ratio of the peak intensity of Fe^{2+} (709.6 eV) to that of Fe^{3+} (708.2 eV) was observed (from 0.24 to 0.40) in the Fe 2p XPS spectra after power generation, providing evidence for the electrochemical reduction of BG to PB.[20,21]

CV measurements were conducted to further investigate the redox reaction. Fig. 3e shows the CV curves of BGC–NC and GC–NC at 90% RH. While GC–NC exhibited no distinct peaks associated with redox reactions, BGC–NC showed notable peaks corresponding to the reduction of BG to PB (−0.55 V) and the oxidation of PB back to BG (0.6 V). These results confirm that the difference in the open-circuit voltage between BGC–NC
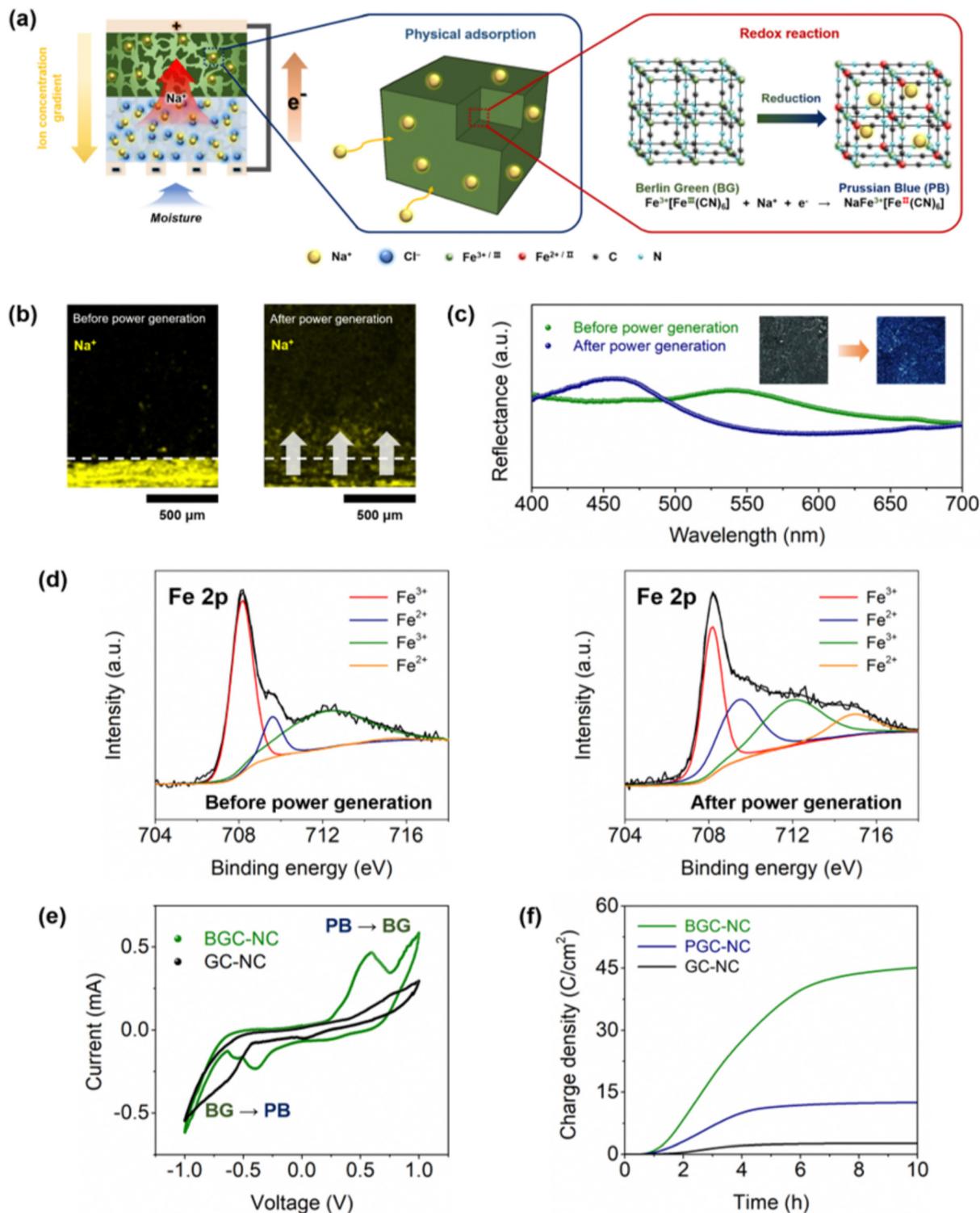
5424 | *Energy Environ. Sci.*, 2024, **17**, 5421–5428

This journal is © The Royal Society of Chemistry 2024

Fig. 3 (a) Schematic illustration of the MEET mechanism of BGC–NC. (b) Cross-sectional EDS mapping images of the BGC–NC layer before (left) and after (right) current generation. (c) UV-visible light reflectance spectra of the BGC layer before (green) and after (blue) current generation. The insets show the images of the BGC layer before and after the current generation. (d) Fe 2p XPS spectra of the BGC layer before (left) and after (right) current generation. (e) CV curves of BGC–NC (green) and GC–NC (black) at 90% RH (scan rate: 1 mV s^{-1}). (f) Time-dependent changes in the accumulated charge densities of BGC–NC (green), PGC–NC (blue), and GC–NC (black) over 10 h under 90% RH conditions.

(1.17 V) and PGC–NC (0.65 V) is attributable to the contribution of the electrochemical reduction reaction. Fig. 3f shows the changes in the accumulated charge densities of GC–NC, PGC–NC, and BGC–NC for over 10 h at 90% RH. The charge density

of BGC–NC accumulated over 10 h (45.1 C cm^{-2}) was 3.6 times higher than that of PGC–NC (12.5 C cm^{-2}); the difference (32.6 C cm^{-2}) is attributed to the faradaic current. Furthermore, the charge density of PGC–NC (12.5 C cm^{-2}) was five times higher than that of GC–NC (2.6 C cm^{-2}), indicating that PB or BG frameworks provide additional physical adsorption sites for Na$^+$ ions.

Impact of RH and BG content on MEET performance of BGC–NC

The influence of RH and BG content on the MEET performance of BGC–NC was investigated. Fig. 4a shows the changes in the maximum voltage and current outputs of BGC–NC at various RH levels of 45–90%. The voltage output increased with the RH owing to the formation of additional Na$^+$ ions and water paths that facilitated ion transport, reaching its peak (1.28 V) at 90% RH. Similarly, the current output increased as the RH increased, reaching 2910 μA cm^{-2} at 90% RH (Fig. S5, ESI†). Fig. 4b shows the variations in the maximum voltage and current density of BGC–NC at 90% RH as functions of the BG content. The BG:CNF weight ratio in the BGC layer ranged from 0 (BGC0–NC or GC–NC) to 6 (BGC6–NC), while the GO and CNF amounts remained constant. Both the voltage and current density increased as the BG content increased, confirming the benefit of BG for power generation. Notably, the charge density exhibited a linear increase as the BG content increased, indicating that the MEET performance of BGC–NC had not yet reached its maximum performance. However, as the BG content increased further, the mechanical stability of the BGC layer was compromised owing to a decrease in the binder material (CNF) content. To evaluate the influence of BGC layer thickness on MEET performance, control experiments were conducted to measure the voltage and current outputs of BGC–NCs with four different BGC layer thicknesses (0.3 mm, 0.6 mm, 1.1 mm, 2.2 mm), while keeping the NC layer thickness fixed at 0.2 mm (Fig. S6, ESI†). Although the voltage output was nearly constant as the BGC layer thickness increased, the current output increased and then saturated at a BGC layer thickness of 1.1 mm. In contrast, when the thickness of the BGC layer was kept constant while varying that of the NC layer, the changes in the voltage and current outputs were negligible (Fig. S7, ESI†), indicating that the NC layer contains excess Na$^+$ ions.

A control experiment was conducted to investigate the influence of GO on MEET performance. When a BG/CNF (BC) composite layer was used in place of the BGC layer, BC–NC exhibited a negligible current output compared to BGC–NC (Fig. S8, ESI†). This result highlights the role of GO as a conductive material that enhances power generation by facilitating electron transfer both near the collecting electrode and throughout the BGC layer. Fig. 4c compares the voltage and current outputs of BGC–NC with values reported in the literature. The current density of BGC–NC significantly surpasses that of all previously reported MPG devices with continuous outputs.[3,6,11,13,14,22–32] It is worth noting that since BGC–NC has a very small thickness (∼1 mm), its voltage output can be easily increased by stacking the device in series without causing a substantial increase in size.

Series configuration and practical applications of BGC–NC devices

Fig. 5a shows a photograph of the device with four BGC–NCs connected in series. Each BGC–NC (6 mm × 6 mm × 1.3 mm) was positioned between two acrylic plates and displayed alongside a commercial R20 battery for size comparison. The open-circuit voltage increased linearly from 1.13 V to 5.55 V as the number of BGC–NCs connected in series increased from 1 to 5 (Fig. 5b). To demonstrate the advantage of the high outputs of the BGC–NC, a series of experiments was conducted. Fig. 5c shows that two BGC–NCs were adequate to power a digital calculator with a power consumption of 200 μW. When a 2000 μF capacitor was connected to three BGC–NCs, the BGC–NCs exhibited a much faster charging rate and reached a higher voltage than the GC–NCs (i.e., conventional MPG), which each had a short-circuit current density of 283 μA cm^{-2} (Fig. S9, ESI†). Furthermore, five BGC–NCs placed inside a natural humidifier were able to activate a filament LED that had an onset voltage of 2.3 V (Fig. 5d) and a UV LED with an onset voltage of 2.9 V (Fig. 5e). Note that the light intensity of the UV LED powered by BGC–NCs was much higher than that of the GC–NCs and sufficient to exhibit an antibacterial effect, highlighting the significance of the high electrical performance of BGC–NC. To investigate the antibacterial effect of the UV LED in a natural humidifier, the UV LED was connected to five BGC–NCs and placed inside the plastic container of the
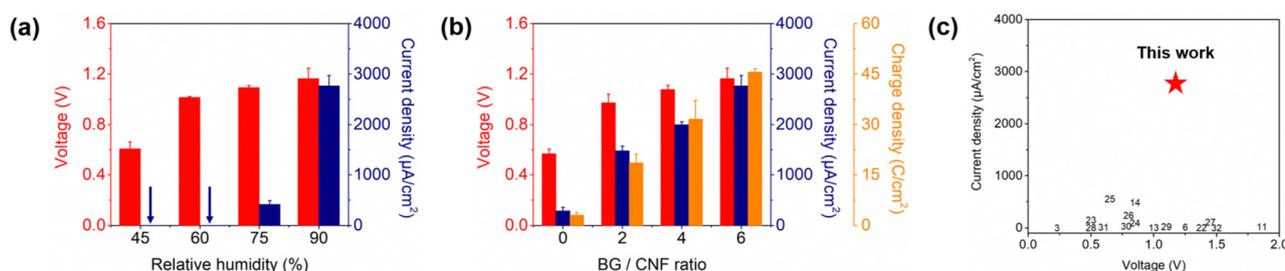

Fig. 4 (a) Changes in the maximum voltage (red) and current density (blue) of BGC–NC at various RH levels. (b) Changes in the maximum voltage (red), current density (blue), and charge density (orange) of BGC–NC at 90% RH as functions of the BG:CNF ratio (w/w) in the BGC layer. The BGC–NC with a BG:CNF ratio of 0 corresponds to GC–NC. (c) Comparison of the voltage and current density outputs of our MPG and previously reported MPG devices that exhibited continuous outputs. The number indicates the reference number.
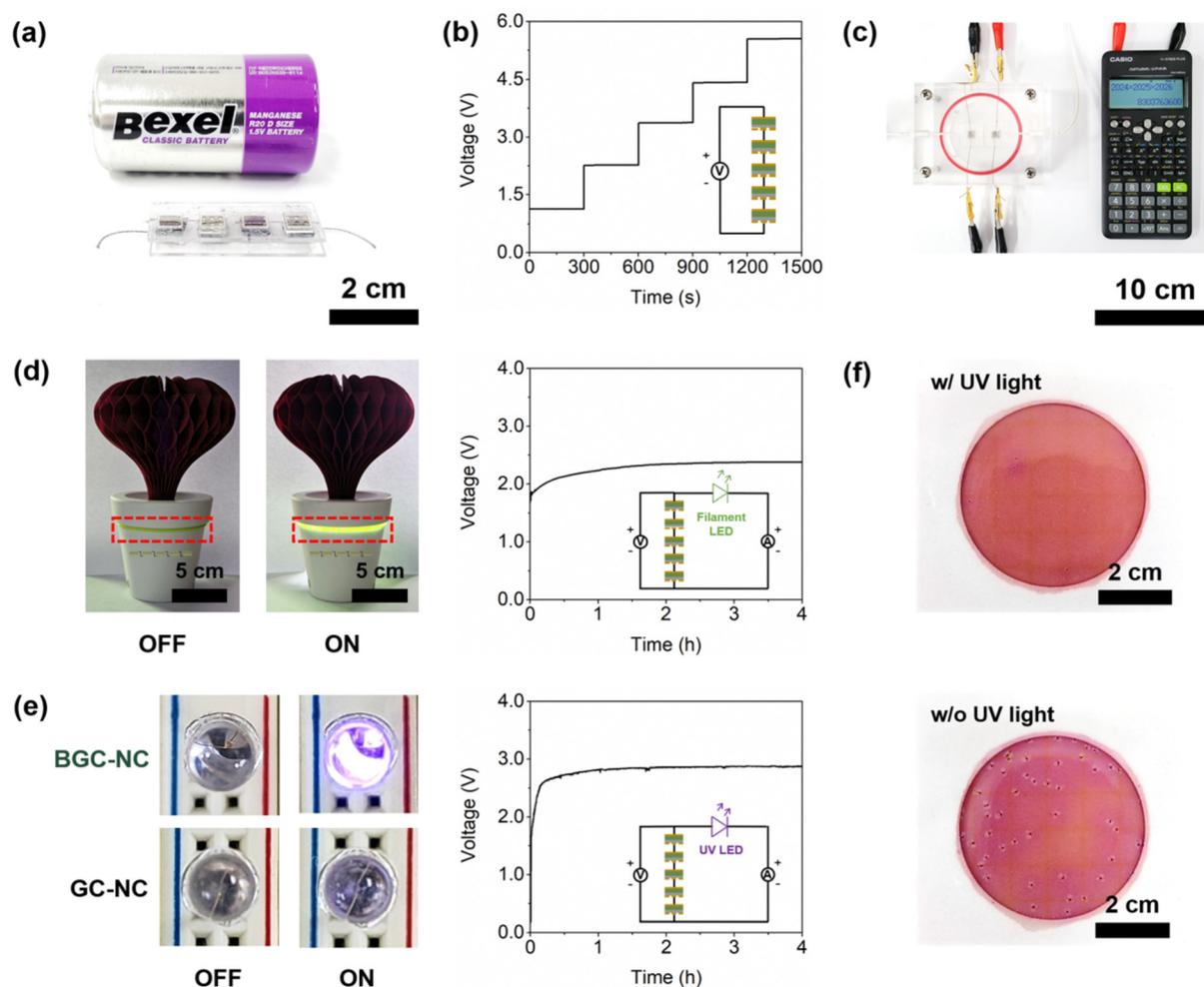
Fig. 5 (a) Photographs of four BGC−NCs connected in series and a commercial R20 battery for size comparison. (b) Time-dependent changes in open-circuit voltage as the number of BGC−NCs connected in series increases. (c) Photograph of the digital calculator powered by two BGC−NCs in series. (d) Photograph of the filament LED activated by five BGC−NCs (left) and time-dependent changes in the voltage output of the five BGC−NCs (right) during the humidification process. (e) Photographs of the UV LED activated by five BGC−NCs (upper) and five GC−NCs (lower), and time-dependent changes in the voltage output of the five BGC−NCs (right) during the humidification process. (f) Photographs of Petrifilms spiked with *E. coli* solution, both with (upper) and without (lower) UV light irradiation during the humidification process.

humidifier containing water spiked with 50 CFU mL^{-1} of *E. coli* O157:H7. After a 5 h humidification process, during which the UV LED was activated, the bacterial solution was spiked on a Petrifilm and incubated for 12 h. Fig. 5f shows the photographs of the Petrifilms spiked with the *E. coli* solution and treated with and without UV light irradiation during the humidification process. Only 4 CFU of *E. coli* were observed in the sample subjected to UV light irradiation, while 48 CFU of *E. coli* were observed in the sample not subjected to UV light irradiation, indicating an antibacterial efficiency of 92%. These results, which were obtained without any capacitors, demonstrate the viable potential of BGC−NC as a power source for various portable electronic devices.

Conclusions

In summary, we have developed a novel MPG that can generate both faradaic and non-faradaic currents by employing BG as an active material. The BGC–NC bilayer was prepared by stacking a BGC layer on an NC layer. When moisture is adsorbed onto the NC layer, the sodium ions dissociate and migrate into the BGC layer, enabling them to be physically adsorbed and inserted into the BG framework. The physical adsorption of positive sodium ions onto the BGC layer results in non-faradaic currents, while the insertion of sodium ions into the BG framework results in faradaic currents through electrochemical reduction, converting chemical energy into electrical energy. This synergistic effect improved the power generation of BGC–NC, resulting in a voltage and current density of 1.17 V and 2770 μA cm^{-2}, respectively, at 90% RH. Notably, BGC–NC is the first MPG to achieve both voltage and current outputs exceeding 1 V and 1 mA cm^{-2}, respectively. It also has the highest current density among the MPG devices with continuous outputs reported thus far. We also demonstrated the applicability of BGC–NC by employing it to activate a digital calculator and a UV LED for antibacterial applications without

This journal is © The Royal Society of Chemistry 2024

Energy Environ. Sci., 2024, **17**, 5421–5428 | **5427**

using any capacitors or rectifiers. These results not only pioneer new directions in the MPG field but also highlight the potential of the developed MPG for commercial viability.

Author contributions

M. S. contributed conceptualization, methodology, investigation, validation, visualization, writing – original draft, and writing – review & editing. D. K. contributed methodology, investigation, validation, visualization, writing – original draft, and writing – review & editing. H. L. and H. H. contributed methodology and investigation. S. J. contributed conceptualization, supervision, writing – original draft, writing – review & editing, funding acquisition, project administration, and resources.

Conflicts of interest

There are no conflicts to declare.

Acknowledgements

References

1 B. Shao, Y. Song, Z. Song, Y. Wang, Y. Wang, R. Liu and B. Sun, *Adv. Energy Mater.*, 2023, **13**, 2204091.

2 P. Guan, R. Zhu, G. Hu, R. Patterson, F. Chen, C. Liu, S. Zhang, Z. Feng, Y. Jiang, T. Wan, L. Hu, M. Li, Z. Xu, H. Xu, Z. Han and D. Chu, *Small*, 2022, **18**, e2204603.

3 S. Lee, H. Jang, H. Lee, D. Yoon and S. Jeon, *ACS Appl. Mater. Interfaces*, 2019, **11**, 26970–26975.

4 D. Kim, J. Eun, J. Ahn, C. Yim and S. Jeon, *ACS Appl. Electron. Mater.*, 2023, **5**, 5938–5943.

5 Y. Li, J. Cui, H. Shen, C. Liu, P. Wu, Z. Qian, Y. Duan and D. Liu, *Nano Energy*, 2022, **96**, 107065.

6 K. Fan, X. Liu, Y. Liu, Y. Li, X. Liu, W. Feng and X. Wang, *Nano Energy*, 2022, **91**, 106605.

7 Z. Sun, L. Feng, X. Wen, L. Wang, X. Qin and J. Yu, *Mater. Horiz.*, 2021, **8**, 2303–2309.

8 Y. Wu, B. Shao, Z. Song, Y. Li, Y. Zou, X. Chen, J. Di, T. Song, Y. Wang and B. Sun, *ACS Appl. Mater. Interfaces*, 2022, **14**, 19569–19578.

9 F. Zhao, Y. Liang, H. Cheng, L. Jiang and L. Qu, *Energy Environ. Sci.*, 2016, **9**, 912–916.

10 Y. Liang, F. Zhao, Z. Cheng, Y. Deng, Y. Xiao, H. Cheng, P. Zhang, Y. Huang, H. Shao and L. Qu, *Energy Environ. Sci.*, 2018, **11**, 1730–1735.

11 C. Liu, S. Wang, X. Wang, J. Mao, Y. Chen, N. X. Fang and S.-P. Feng, *Energy Environ. Sci.*, 2022, **15**, 2489–2498.

12 P. Wang, J. Xu, R. Wang and T. Li, *Cell Rep. Phys. Sci.*, 2023, **4**, 101517.

13 W. He, H. Wang, Y. Huang, T. He, F. Chi, H. Cheng, D. Liu, L. Dai and L. Qu, *Nano Energy*, 2022, **95**, 107017.

14 H. Zhang, N. He, B. Wang, B. Ding, B. Jiang, D. Tang and L. Li, *Adv. Mater.*, 2023, **35**, e2300398.

15 J. Bai, Y. Huang, H. Wang, T. Guang, Q. Liao, H. Cheng, S. Deng, Q. Li, Z. Shuai and L. Qu, *Adv. Mater.*, 2022, **34**, e2103897.

16 F. S. Hegner, J. R. Galan-Mascaros and N. Lopez, *Inorg. Chem.*, 2016, **55**, 12851–12862.

17 J. Y. Heo, J.-H. Lee, J.-G. Bae, M. S. Kim, H. J. Lee and J. H. Lee, *Green Chem.*, 2023, **25**, 6823–6831.

18 X. Wu, W. Deng, J. Qian, Y. Cao, X. Ai and H. Yang, *J. Mater. Chem. A*, 2013, **1**, 10130.

19 Z. Shadike, D.-R. Shi, T.-W. Tian-Wang, M.-H. Cao, S.-F. Yang, J. Chen and Z.-W. Fu, *J. Mater. Chem. A*, 2017, **5**, 6393–6398.

20 Q. Yang, F. Mo, Z. Liu, L. Ma, X. Li, D. Fang, S. Chen, S. Zhang and C. Zhi, *Adv. Mater.*, 2019, **31**, e1901521.

21 L.-P. Wang, P.-F. Wang, T.-S. Wang, Y.-X. Yin, Y.-G. Guo and C.-R. Wang, *J. Power Sources*, 2017, **355**, 18–22.

22 H. Wang, Y. Sun, T. He, Y. Huang, H. Cheng, C. Li, D. Xie, P. Yang, Y. Zhang and L. Qu, *Nat. Nanotechnol.*, 2021, **16**, 811–819.

23 H. Wang, T. He, X. Hao, Y. Huang, H. Yao, F. Liu, H. Cheng and L. Qu, *Nat. Commun.*, 2022, **13**, 2524.

24 R. Zhu, Y. Zhu, F. Chen, R. Patterson, Y. Zhou, T. Wan, L. Hu, T. Wu, R. Joshi, M. Li, C. Cazorla, Y. Lu, Z. Han and D. Chu, *Nano Energy*, 2022, **94**, 106942.

25 J. Eun and S. Jeon, *Nano Energy*, 2022, **92**, 106772.

26 S. Yang, X. Tao, W. Chen, J. Mao, H. Luo, S. Lin, L. Zhang and J. Hao, *Adv. Mater.*, 2022, **34**, e2200693.

27 R. Zhu, Y. Zhu, L. Hu, P. Guan, D. Su, S. Zhang, C. Liu, Z. Feng, G. Hu, F. Chen, T. Wan, X. Guan, T. Wu, R. Joshi, M. Li, C. Cazorla, Y. Lu, Z. Han, H. Xu and D. Chu, *Energy Environ. Sci.*, 2023, **16**, 2338–2345.

28 X. Liu, H. Gao, J. E. Ward, X. Liu, B. Yin, T. Fu, J. Chen, D. R. Lovley and J. Yao, *Nature*, 2020, **578**, 550–554.

29 Y. Zhang, T. Yang, K. Shang, F. Guo, Y. Shang, S. Chang, L. Cui, X. Lu, Z. Jiang, J. Zhou, C. Fu and Q. C. He, *Nat. Commun.*, 2022, **13**, 3484.

30 J. Tan, S. Fang, Z. Zhang, J. Yin, L. Li, X. Wang and W. Guo, *Nat. Commun.*, 2022, **13**, 3643.

31 K. Zhao, J. W. Lee, Z. G. Yu, W. Jiang, J. W. Oh, G. Kim, H. Han, Y. Kim, K. Lee, S. Lee, H. Kim, T. Kim, C. E. Lee, H. Lee, J. Jang, J. W. Park, Y. W. Zhang and C. Park, *ACS Nano*, 2023, **17**, 5472–5485.

32 Y. Huang, H. Cheng, C. Yang, P. Zhang, Q. Liao, H. Yao, G. Shi and L. Qu, *Nat. Commun.*, 2018, **9**, 4166.

5428 | *Energy Environ. Sci.*, 2024, **17**, 5421–5428

This journal is © The Royal Society of Chemistry 2024